Interaction between Catalyst and Support. 4. Periodic Trends and Patterns in Interactions of First-Row Transition Metals with the Silica Surface

Qisheng Ma and Kamil Klier*

Department of Chemistry and Zettlemoyer Center for Surface Studies, Lehigh University, Bethlehem, Pennsylvania 18015

Hansong Cheng* and John W. Mitchell

Air Products and Chemicals, Inc., 7201 Hamilton Boulevard, Allentown, Pennsylvania 18195-1501

Received: February 20, 2002; In Final Form: July 18, 2002

A "double-hump" pattern and a systematic trend of adsorption energies of the first-row transition metal atoms (Ca, Sc, Ti, V, Cr, Mn, Fe, Co, Ni, Cu, Zn), adsorbed on the surface of silicon dioxide, has been revealed by all-electron density functional theory (DFT) calculations. The study employs periodic DFT at the full-potential linearized augmented plane wave (FP-LAPW) level with spin-polarization taken into account. The geometry of the adsorbed atoms and the silica surface is optimized. The double-hump dependence of the neutral metal adsorption energy on the number of d electrons is reminiscent of the ligand field stabilization energy (LFSE) pattern for ions, but superimposed on it are significant contributions involving 4s electrons of neutral atoms. As a result, the overall trend for neutral atoms is to decrease adsorption strength (or adhesion) with increasing atomic number on top of the Ar closed shell, and this trend is opposite to that of ions that are bonded with increasing strength as the number of electrons in the $[Ar]3d^n4s^{1-2}$ series increases.

1. Introduction

The study of interactions between transition metals and oxides is of great importance both theoretically and experimentally.[1] For decades, the semiempirical ligand field theory (LFT) approach has been successfully applied to predict and interpret energetic relationships and optical and magnetic properties in these open-shell, multiple-bonded systems. One of the major successes of the LFT theory is the agreement between the prediction of the periodic "double-hump" energy pattern in aquo complexes due to the ligand field stabilization energy (LFSE), or crystal field stabilization energy (CFSE), introduced by Penney,[2] and the experimental lattice energies of $Me^{II}O$ oxides (Me = Ca, Ti, V, Mn, Fe, Co, Ni, Cu, Zn) reported by Hush and Pryce.[3] The redistribution of 3d electrons among partially filled d orbitals split in the ligand field of nearest neighbor atoms or ions, combined with electronic exchange effects via perturbation theory, has led to the understanding of a large number of low-lying configurations and electronic states.

The rapidly developing density functional theory (DFT), by implicitly incorporating the electron correlation and exchange correlation effects, is believed to have a much greater potential than standard quantum chemical methods for large (transition metal) systems.[4] Several high-level DFT calculations performed on various relatively simple systems involving first-row transition metals have produced satisfactory agreement between the DFT, LFT, and experimental measurements. Among these, Wang and Schwarz[5] studied first-row transition metal dihalides using the Amsterdam density functional program ADF, Bridgeman and Rothery[6] used the "DeFT" code in the linear combination of Gaussian-type orbitals (LCGTO) framework to study periodic trends in diatomic monoxides and monosulfides of the 3d transition metals, and our recent full-potential linearized augmented plane wave (FP-LAPW) calculations[7] of lattice energies of $Me^{II}O$ oxides (Me = Ca, ..., Zn) have shown a quantitative agreement with experiment and a qualitative agreement with the semiempirical LFT picture. All these studies provide significant support for the physical identity of the LFT and DFT theories. However, the level of DFT employed, particularly in systems with transition metals, is important for accuracy and correct account of properties. A significant role is played by the basis set including functions describing electron density in the open space, by the choice of the functional, by taking into account relativistic effects, and by using periodic conditions for periodic structures.

Up to now, most theoretical calculations had focused on either gas-phase molecules or perfect solid crystals, in which transition metals exist in their +2 formal valence state. Challenges remain for more complex systems, particularly for systems that involve 4s electrons from neutral transition metals. From the theoretical point of view, orbital energies of the 4s orbitals lie close to those of the 3d orbitals to form the s−d hybrids.[8,9] The presence of 4s electrons in neutral atoms would be expected to interact with 3d electronic configurations, resulting in a more complicated interaction pattern throughout the whole series than in a series of ionic compounds devoid of the 4s valence electrons.

From the practical point of view, transition metals supported on oxides are of importance in a variety of industrial applications. Among these, interactions between transition metals and supporting oxides are of special interest as they determine the efficiency of composite catalysts in many chemical reactions. Our previous calculations[10−12] on the interaction of Co and Ni atoms and clusters on silica and alumina surfaces have indicated that the interaction between the diffuse 4s electrons with the Si-3s and Al-3s orbitals in the substrates is the dominant adhesion force. The questions remain whether this is a general phenomenon throughout the whole first transition series

10.1021/jp020479c CCC: $22.00
Published on Web 09/04/2002

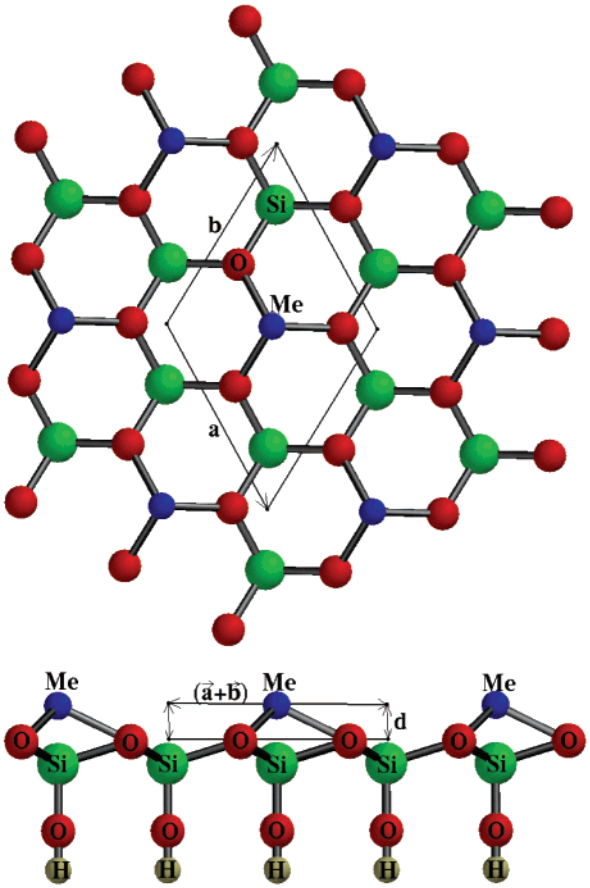

Figure 1. Structure of the periodic $[MeSi_2O_3(OH)_2]_{\infty,\infty}$ slab model: (top) a two-dimensional unit cell with hexagonal primitive lattice translations *a* and *b*; (bottom) a side view showing the elevation *d* of the Me atom above the plane of the siloxane oxygens. The geometry was optimized for each Me atom as described in section 3.1.

and how the presence of 4s electrons affects the periodic trend and pattern of the metal−oxide interaction energies. On the basis of the FLAPW-DFT periodic spin-polarization calculations, the periodic patterns of the adhesion energies of the first transition series (Ca, ..., Zn) on the silica surface are presented herein.

2. Computational Details

The model employed in the present calculations is essentially that used in our earlier calculations of adsorption energies of Co and Ni[10] and is represented in Figure 1.

The model for the siloxane silica surface in Figure 1 is a modified β-cristobalite (111) slab consisting of an Si−O−Si stacking sequence, with an additional H-layer at the bottom to keep the slab charge neutral. The slab has a hexagonal structure of repeating unit cells of stoichiometry $O_{3(top)}Si_2(OH)_2$ with fixed dimensions $|a| = |b| = 0.53$ nm and $c \perp (a, b)$, $|c| = 1.5$ nm, large enough to prevent appreciable interactions between the slabs. The internal atomic coordinates were optimized using a damped Newton scheme under the criterion that requires all the forces acting upon the atoms be less than 10 mRy/au.[10]

The all-electron DFT calculations were performed using the WIEN97.9 code with the full-potential linearized augmented plane wave (FP-LAPW) method.[13] The Kohn−Sham (KS) equations[14] are solved self-consistently in an iterative process under the generalized gradient approximation (GGA) with the Perdew−Burke−Ernzerhof (PBE) functional for the exchange-correlation energy,[15,16] subject to periodic lattice boundary conditions. The matrix elements overlap $S_{\mathbf{k},\mathbf{k}'} = \langle\phi_{\mathbf{k}}|\phi_{\mathbf{k}'}\rangle$ and Hamiltonian $H_{\mathbf{k},\mathbf{k}'} = \langle\phi_{\mathbf{k}}|H|\phi_{\mathbf{k}'}\rangle$ are evaluated and diagonalized to obtain eigenvalues and eigenvectors of the K−S orbitals, where $\phi_{\mathbf{k}}$ are the basis set functions whose numbers determine the size of the matrix. The present calculations involving transition metals are carried out in an unbiased spin-polarized mode as in our earlier work,[10−12] wherein the spin-up and spin-down densities are calculated separately, using the PBE functional.[15] Computational details used in this work were the same as those in our previous calculations of Co and Ni adsorption on silica surface[10]—a modified tetrahedron integration scheme was used to generate the **k**-mesh in the irreducible wedge of the hexagonal Brillouin zone on a special grid of (2 × 2 × 1) **k**-points, the energy cutoff was 20 Ry, and 50 000 plane waves were generated to simulate the interstitial region and were augmented inside the atomic ("muffin tin") spheres of radius R_{MT} by linear combinations of radial functions and spherical harmonics.[10−13] Because the present approach utilizes periodic boundary conditions, the energies of free atoms, which are necessary for the description of the initial state prior to adsorption, were also calculated on a periodic model in which each metal atom was placed in a large, periodically repeating box. Further assessment of the accuracy of energy calculation for various choices of the box size and details of plane wave cutoffs for the free "atoms in a box" are given in section 3.2.

In practice, only a finite number of plane waves is used. A *cutoff energy* E_{cutoff} in the units of Ry is usually set to truncate all plane waves with $(\mathbf{k} + \mathbf{K}_n)^2 > E_{cutoff}$, where **k** is the wave vector inside the first Brillouin Zone (BZ), and $\mathbf{K}_n$ are the reciprocal lattice vectors. In the WIEN code,[13] the matrix size is determined by an input parameter $R_{MT}K_{MAX}$, where K_{MAX} is the magnitude of the largest $\mathbf{K}_n$ vector, or the so-called "plane wave cutoff" and R_{MT} is the smallest of all atomic sphere radii inside the unit cell (in au unit). The matrix size, however, is constrained by the matrix dimension NMAT that is user predefined in the WIEN program during compilation. Therefore, the actual matrix size of calculations is determined by whatever is smaller, the input plane wave cutoff (specified with $R_{MT}K_{MAX}$) or the matrix dimension NMAT (which defines the computational size depending on computational resources).

3. Results and Discussion

3.1. Geometry of Adsorbed Metals. The internal atomic coordinates of the silica slab were fully optimized before the metal adsorption using the damped Newton method. A single neutral metal atom of the first transition series Me = Ca, Sc, Ti, V, Cr, Mn, Fe, Co, Ni, Cu, and Zn has been adsorbed onto the 3-fold oxygen adsorption site in each unit cell, corresponding to the Me:$O_{(top)}$ ratio 1:3. The surface $O_{(top)}$ layer and second Si layer were allowed to relax with metal adsorption, whereas the dangling (OH) groups were fixed.

In the most stable geometric configurations, metal atoms above the 3-fold oxygen sites settled at the metal−oxygen distance between 0.190 and 0.240 nm, comparable with the experimentally observed ionic metal(II)−oxygen bong lengths in compact oxides.[3] Figure 2 summarizes the calculated metal−oxygen distances compared with the experimental metal(II)−oxygen bond lengths in the compact oxides. The vertical distances of the metal atoms to the oxygen plane are also shown. The double-hump pattern of the metal−oxygen distances experimentally observed for "divalent ions" is clearly replicated by the calculated distances of *neutral* metal atoms from both the nearest oxygen atoms and along an outward normal to the oxide surface. The contraction of these distances is largest for

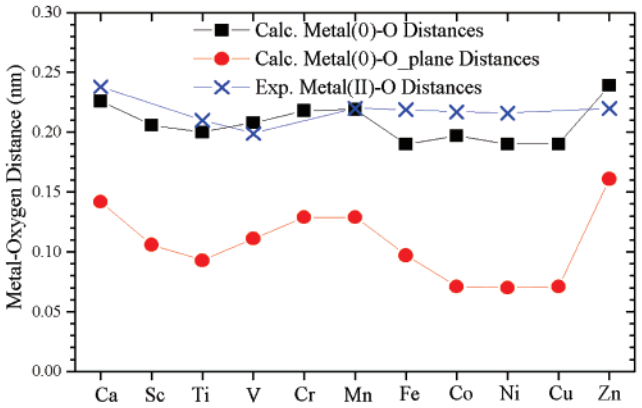

Figure 2. Comparison of metal−oxygen distances of adsorbed neutral atoms on the 3-fold oxygen hollow sites and the experimental metal-(II)−oxygen distances.[3] Vertical distances of metals to the nearest oxygen plane are also shown.

Ti^0, Ni^0, and Cu^0, roughly correlating with the behavior of the corresponding Me(II) "ions" in compact oxides. This distance pattern therefore appears to be dominated by the partially filled 3d shells. The 4s electrons of the neutral species Me^0 are delocalized into bonds through the interstitial space to the Si atoms of supporting oxide and will be shown below to significantly contribute to the adsorption energy.

3.2. Metal Atoms in a Box. The adsorption energy ΔE of the neutral atoms is defined as

$$\Delta E = E_{\mathrm{Me+slab}} - (E_{\mathrm{slab}} + E_{\mathrm{Me}}) \qquad (1)$$

where $E_{\mathrm{Me+slab}}$ is the total calculated energy of the unit cell containing the adsorbed metal atom in its equilibrium position, E_{slab} is that of the slab alone, and E_{Me} is the total calculated energy of a single metal atom that is computed by locating a single Me^0 atom in a large empty cubic box. Evaluation of the adsorption energy ΔE by eq 1 relies on an accurate calculation of the atomic energy E_{Me} and a careful correlation of computational conditions on three independently calculated energies. The convergent test of calculated atomic energies with respect to the dimension of the empty box and computing parameters is crucial.

In general, the calculated atomic energies should converge to a steady value upon gradually increasing the unit cell dimension as the artificial cell−cell interactions are being reduced. However, a big unit cell requires a large basis set of plane waves, resulting in a demand of large matrix size. Figure 3 illustrates effects of the unit cell size as well as the matrix dimension (NMAT) on the calculated atomic energy. In the small unit cell range (unit cell dimensions 0.5 ∼ 0.7 nm), the "actual plane wave cutoff", K_{MAX} (given in Figure 3 by numbers inside the parentheses for each calculation), remains close to the input value $R_{\mathrm{MT}}K_{\mathrm{MAX}} = 8.00$, where the "muffin tin radius" R_{MT} is given in Bohr (au) = 0.0529 nm and K_{MAX} in $\mathrm{Ry}^{1/2}$. The increase of the calculated atomic energy with the cell dimension is mainly due to the reduction of the cell−cell interaction. Consequently, changing NMAT did not affect the calculated result, as there are sufficiently large matrix sizes for enough plane waves to fit in.

However, for large unit cells (unit cell dimensions 0.8−1.0 nm), the "actual plane wave cutoff" had been automatically reduced in the execution of the program because of insufficient matrix size constrained by smaller NMAT values. The incomplete basis set effect had then dominated the computational accuracy. For instance, the calculated atomic energy, with a fixed NMAT = 3300, did not converge with increasing cell dimensions. To achieve a convergent result as indicated in Figure 3 by a thick fitting line, NMAT needs to be maintained sufficiently large to keep K_{MAX} values close to the input $R_{\mathrm{MT}}K_{\mathrm{MAX}} = 8.00$.

The advantage of using plane wave basis sets in the FP-LAPW approach is the possibility of testing the convergence by including more plane waves to reduce the incomplete basis set effects at a higher cost of computational resources. For a Cr^0 atom in a 1.0 × 1.0 × 1.0 nm^3 cubic cell, the calculated atomic energy converges to a stable value with increasing "actual plane wave cutoff" K_{MAX} value (including plane waves), as shown in Figure 4. Furthermore, the atomic energy of the Cr^0 atom converges to the same value, −2101.47 Ry, as shown in Figure 3 with respect to the increases of both cubic box dimensions and the plane wave cutoff K_{MAX}.

3.3. Adsorption Energies. To obtain the reliable adsorption energy, one needs to consider the computational accuracy for the slab and metal + surface systems as well. For systems involving more than one type of atom with different muffin-tin radii, the plane wave cutoff K_{MAX} is determined by the smallest R_{MT}. The atomic sphere radii used in our calculations are listed in Table 1.

For systems involving hydrogen with short bond lengths to its neighbors, a relatively small muffin-tin radius $R_{\mathrm{MT}} \equiv R_{\mathrm{H}} = 0.7$ au for the H atom is used in both the surface slab and metal + surface systems. In these calculations, the matrix size NMAT was set to 3300, resulting in an actual calculated $R_{\mathrm{H}}K_{\mathrm{MAX}} = 2.64$, giving rise to a value of the plane wave cutoff $K_{\mathrm{MAX}} = 3.77$. For the purpose of using eq 1 to evaluate the adsorption energies under comparable computational accuracy conditions, we seek a close K_{MAX} value for the atomic energy calculations with a single metal atom inside a sufficiently large empty cubic cell. This value falls in the ranges of the 0.8 nm unit cell with NMAT = 3300 ($K_{\mathrm{MAX}} = 3.83$), the 0.9 nm unit cell with NMAT = 4400 ($K_{\mathrm{MAX}} = 3.73$), and the 1.0 nm unit cell with NMAT = 6600 ($K_{\mathrm{MAX}} = 3.61$) (viz. Figure 3). Therefore, instead of using the convergent, but over-accurate atomic energies, we used the atomic energies calculated with the plane wave cutoff K_{MAX} consistent with those in the surface slab and metal-surface systems.

The atomic energies of first-row transition metals calculated under these three conditions are listed in Table 2. The standard deviations (S.D.) for all atomic energies are on the order of 0.010 Ry (∼0.2 eV). This suggests that unit cell dimensions in the ranges 0.8−1.0 nm are in general sufficiently large to prevent artificial effects of periodic arrangements and the plane wave cutoff is the key factor in determining the computing accuracy. The average atomic energy of the Cr atom, −2101.45 Ry (viz. Table 2), is by 0.02 Ry (0.3 eV) higher than the convergent limit of the calculated atomic energy, −2102.47 Ry (viz. Figures 3 and 4). The adsorption energies calculated with the use of eq 1 where E_{Me} are the average atomic energies, E_{slab}, the slab energies, and $E_{\mathrm{Me+slab}}$, the adsorbed atom energies with optimized geometry, are illustrated in Figure 5a.

3.4. Contributions by 4s Electrons. One of the striking features of the adsorption energy pattern of neutral atoms (Figure 5a) is the uphill trend (decreasing adhesion force) throughout the whole series. This is in contrast to the well-known downhill trend pattern of the adsorption energies of Me(II) in oxygen six-ring windows of zeolite LTA calculated according to

$$\Delta E_{\mathrm{lattice}} = E_{\mathrm{Me(II)-LTA}} - [E_{\mathrm{LTA}}{}^{2-} + E_{\mathrm{Me(II)}}] \qquad (2)$$

Here $E_{\mathrm{Me(II)-LTA}}$ has two contributions, a lattice energy calcu-

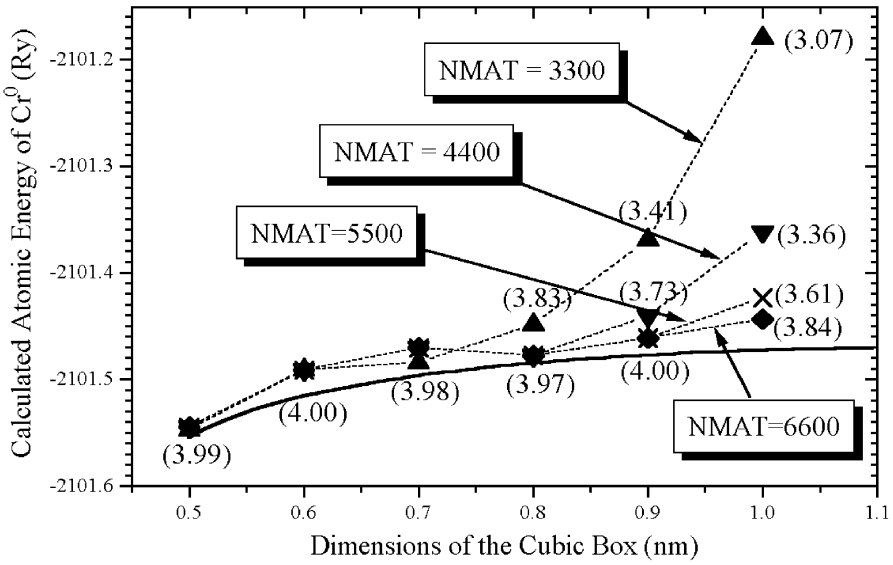

Figure 3. Variation of the total calculated Cr atomic energy inside an empty cubic cell with respect to cell dimensions and the plane wave cutoff (indicated by the number inside the parentheses), which is confined by the predefined matrix size NMAT or the input parameter $R_{MT}K_{MAX} = 8.00$, whichever is smaller. The fitting thick line indicates the convergent atomic energy with the progressively increasing cell dimension under the same plane wave cutoff.

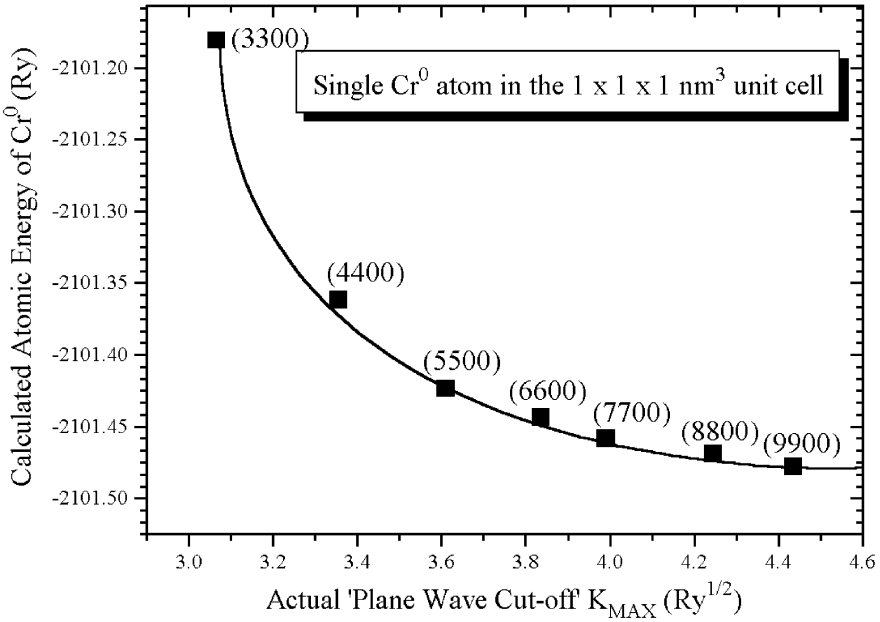

Figure 4. Calculated Cr atomic energy converging with respect to the actual plane wave cutoff, K_{MAX}. The atom is placed inside a $1 \times 1 \times 1$ nm^3 empty cubic cell. The fitting thick line indicates the convergent atomic energy with progressively increasing plane wave cutoff energy.

TABLE 1: Spherical Muffin-Tin Radii of Atoms Used in Calculations

atoms	spherical muffin-tin radius R_{MT} (a.u.)
H	0.7
O	1.0
Si	1.0
transition metal atoms	2.0

lated from spherical contributions of the ion−zeolite bonding energy averaged over ionic and covalent components[17,18] and the ligand field stabilization energies due to nonspherical contributions by the partially filled d shells.[19] The "double hump" pattern is due to the nonspherical contributions, and a large negative portion of the energy is primarily due to the electrostatic Madelung energy. Because there are no interactions between the separated "gas phase" ions in the term [$E_{LTA}{}^{-2}$ + $E_{Me(II)}$], their contributions to the lattice energy is zero[17,18] and $\Delta E_{lattice}$ is the true lattice energy.

In the transition *metal ion* complexes and oxides, 3d electrons from the transition metals are major participants in the metal−ligand interactions. To the first approximation, the localized 3d orbitals determine that the metal−ligand interaction occurs within a short range. When proceeding from the left to the right in the transition series, 3d orbitals are increasingly contracted due to increasing nuclear charge. This results in an overall trend of decreasing distances between the metal ion and the ligands, with a concomitant increase of attractive electrostatic energy, Figure 5b, dashed "background" line.

In the presently studied adsorbed *neutral atoms*, the trend is opposite due to the presence of the 4s electrons, Figure 5a, dashed "background" line. This feature strongly suggests an important role that 4s electrons play in the adsorption of neutral

TABLE 2: Calculated Atomic Energies of First-Row Transition Metal Atoms

	atomic energy (Ry)				
metal	$0.8 \times 0.8 \times 0.8$ nm^3 NMAT=3300	$0.9 \times 0.9 \times 0.9$ nm^3 NMAT=4400	$1.0 \times 1.0 \times 1.0$ nm^3 NMAT=6600	average[a]	S.D.[b]
Ca	−1360.686	−1360.675	−1360.677	−1360.679	0.006
Sc	−1528.166	−1528.155	−1528.160	−1528.160	0.006
Ti	−1707.268	−1707.222	−1707.227	−1707.239	0.025
V	−1898.225	−1898.216	−1898.223	−1898.221	0.004
Cr	−2101.466	−2101.440	−2101.448	−2101.451	0.013
Mn	−2317.006	−2316.995	−2317.003	−2317.001	0.006
Fe	−2545.223	−2545.209	−2545.212	−2545.215	0.007
Co	−2786.546	−2787.539	−2786.540	−2786.542	0.004
Ni	−3041.277	−3041.256	−3041.279	−3041.271	0.013
Cu	−3309.771	−3309.759	−3309.772	−3309.767	0.007
Zn	−3592.127	−3592.115	−3592.126	−3592.123	0.007

[a] Average of atomic energies of three different calculations. [b] Standard deviations with respect to the average atomic energies.

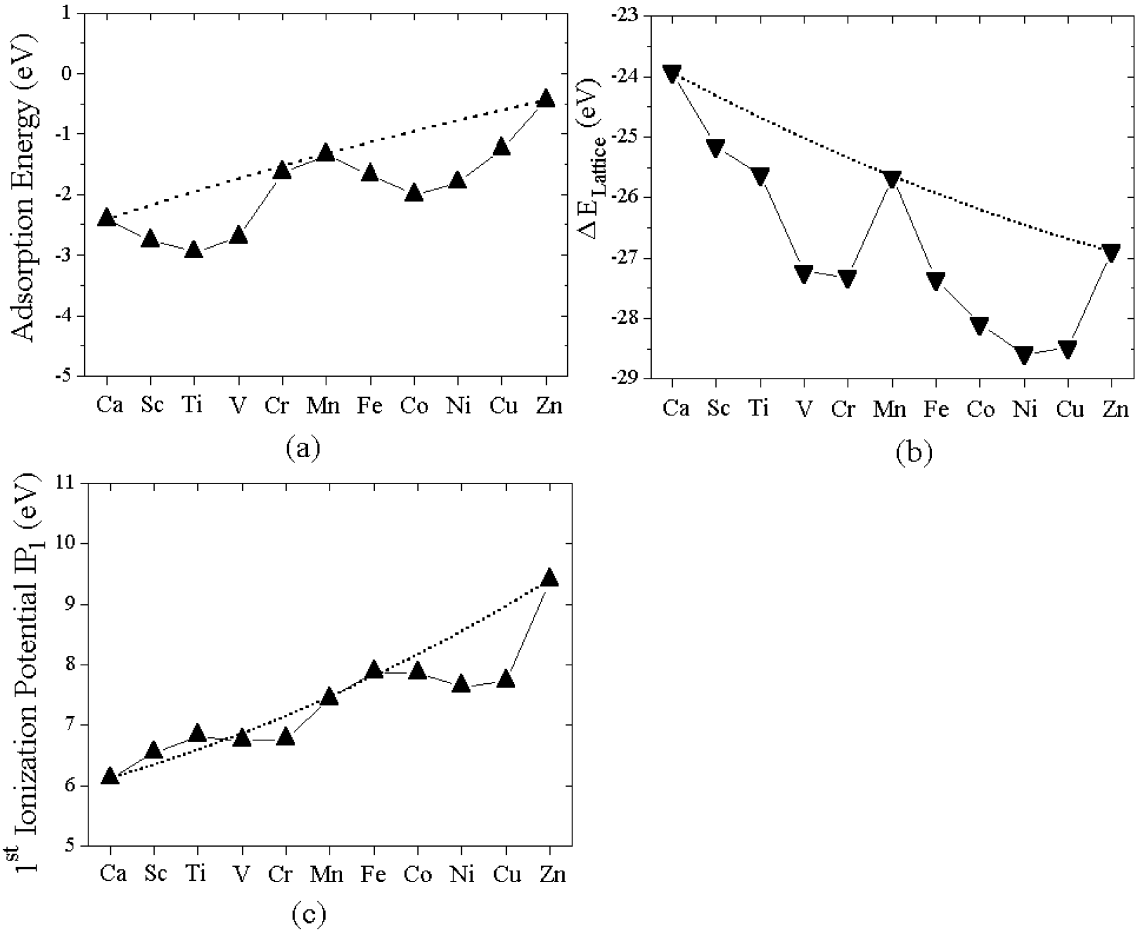

Figure 5. Periodic patterns in oxide-bonded first-row transition metals: (a) adsorption energies of neutral Me(0) on the silica surface in the present calculations; (b) adsorption energies of divalent cations Me(II) into a zeolite matrix from ref 1 as also summarized in text; (c) first ionization potential IP_1 of first-row transition metals Me(0), from ref 16.

metal atoms Me(0). The 4s orbital is much more diffuse than the 3d orbitals and is extended with a long smooth tail to 0.4−0.5 nm. Therefore 4s electrons of first transition series atoms are capable of penetrating to a much longer range to interact with the second nearest neighbors, Si, at an average distance of 0.35 nm. In fact, our previous studies of Co and Ni on SiO_2 indicated that the adsorption energies are dominated by the interaction of the occupied metal 4s electron levels with an empty Si-3s orbital. Consequently, the penetrating ability of a 4s electron determines the strength of transition metal−support interactions, resulting in the uphill trend as the 4s orbital becomes more localized with the increasing nuclear charge. Even though the adsorbed metals remain in their atomic state, the first ionization energy (IP_1) is still a useful parameter that reflects the ability to transfer the first 4s electron of the metal atom to the oxide (Figure 5c). The data for the end members of the series, Ca and Zn, illustrate the case in point: the low ionization energy IP_1 of Ca contributes to the stabilization of the adsorption bond by a facile transfer of its 4s electron to the silica substrate, whereas the high IP_1 of Zn keeps the 4s electron more localized on the metal, resulting in a smaller contribution to the adsorption bond.

The presence of the 4s electrons alters the s−d electronic configuration via the s−d hybridization. A typical example is

TABLE 3: Calculated Net-Spin of Metals in a Box and in the Adsorbed State[a]

	free atoms			
metals	0.8 × 0.8 × 0.8 nm^3	0.9 × 0.9 × 0.9 nm^3	1.0 × 1.0 × 1.0 nm^3	adsorbed
Ca	0.0	0.0	0.0	0.0
Sc	0.5	0.5	0.5	0.2
Ti	2.5	2.0	1.4	0.9
V	2.5	2.5	2.5	1.5
Cr	3.0	3.0	3.0	2.7
Mn	2.5	2.5	2.5	2.5
Fe	2.0	2.0	2.0	2.0
Co	1.5	1.5	1.5	1.4
Ni	1.0	0.0	1.0	0.8
Cu	0.5	0.5	0.5	0.0
Zn	0.0	0.0	0.0	0.0

[a] Net-spin is calculated as half of the sum of net-spin charge inside muffin-tin sphere of metals plus the net-spin charge in the interstitial space.

the adsorption of neutral Cr(0) for which the $3d^5 4s^1$ configuration has been found to be the ground state in both the free atom and the adsorbed state. This promotion from the $3d^4 4s^2$ to $3d^5 4s^1$ configuration results in a substantial difference between bonding of Cr(0) and Cr(II) [$3d^4$], as is apparent from the comparison of relative stabilization energies of these two chromium species in Figure 5a,b. The Cu(0) adsorption occurs from the free atom of configuration $3d^{10}4s^1$ (spin $^1/_2$) to adsorbed atoms with calculated zero spin (Table 3, column 5). Analysis of coefficients of the local orbitals reveals that zero spin originates from mixing of "spin-up" $3d^{10}4s^1$ and "spin-down" $3d^9 4s^2$ rations.

3.5. Contributions by 3d Electrons. The double-hump pattern of the adsorption energies of the neutral 3d metals, Me^0, calculated herein by the DFT method is reminiscent of the pattern of lattice energies of the divalent metal ions, Me^{II}, in zeolite matrixes, previously estimated with the use of the semiempirical ligand field theory (LFT).[1] The most stable site for the metal atom on the presently studied silica surface is a trigonal hollow site made by the nearest three oxygens, and common sites for the metal ions in zeolites are also oxygen trigonal sites. Qualitatively, we can view the neutral metal adsorption energies as due to the interaction of the 3d shell of the ions and the 4s shell that modifies the 3d pattern. With this approach, we are able to simulate the basic features of the DFT pattern by the LFT method, showing that the physical origin of the relative stabilities emerges from both theories, as we have demonstrated previously for compact oxides.[7]

3.5.1. Ligand Field Theory (LFT) Interpretation. The LFT method arrives at the energy patterns with the use of the Racah's parameters B and C, which characterize interelectronic Coulombic and exchange interactions, and the ligand field parameters, which characterize the effects of the bonding/antibonding of the central metal atom with neighbors. For the latter, we have used the parameters γ_{20} and γ_{40}, $\gamma_{k0} = -4\pi e/(2k+1)\int \rho(\mathbf{R})\, Z_{k0}(\Theta,\Phi)/(R^{k+1})\, d\tau$, where $\rho(\mathbf{R})$ is the ligand charge distribution at position $\mathbf{R}$ from central atom, $-e$ is the electron charge, and $Z_{k0}(\Theta,\Phi)$ are real spherical harmonics of the ligand field at angles Θ and Φ. The γ_{k0} parameters originate from an expansion of the ligand field potential, viz. below, using the spherical harmonics addition theorem.[21] The γ_{k0} parameters were converted to $G_2 = \sqrt{5/4\pi}\ \gamma_{20}\langle r^2\rangle$ and $G_4 = \sqrt{9/4\pi}\ \gamma_{40}\langle r^4\rangle$.[19] The value of G_4 is related to the octahedral splitting between the e_g and t_{2g} levels, Δ_0, as $G_4 = {}^5/_6\Delta_0$, and the Δ_0 values are known from spectroscopy or estimated by interpolations. We have used here the following values of G_4 and Racah's B as listed in Table 4.

TABLE 4: Ligand Field Stabilization Energies (LFSE) of Me(II)[a]

ion	G_4 (cm^{-1})	B (cm^{-1})	angle β (deg)
Sc(II)	13600[b]	718[f]	121
Ti(II)	12670[c]	718[g]	118
V(II)	12600[d]	766[g]	122
Fe(II)	10400[d]	1058[g]	121
Co(II)	7900[d]	1115[g]	111
Ni(II)	8500[d]	1084[g]	112
Cu(II)	6300[e]	1238[g]	112

[a] The values for Cr(II), Mn(II), and Zn(II) are not needed here because the neutral atoms have half-filled or filled d-shells in the spherically symmetric configurations Cr[$3d^5 4s^1$], Mn[$3d^5 4s^2$], and Zn[$3d^{10}4s^2$] and are not stabilized by nonspherically symmetric redistribution of the d electrons in the ligand field. [b] Ti(III)*2/3, from ref 20. [c] V(III)*2/3, from ref 20. [d] Reference 21, p 302. [e] Reference 21, p 302, half of the value for Jahn−Teller distorted octahedral complexes as discussed by Griffith. [f] The value for Ti(II) was taken here in the absence of known value for Sc(II). [g] Reference 21, Table 6.1, p 437.

The LFT calculations of the stabilization energies were performed by simultaneous diagonalization of matrices of the ligand field $V_{LF} = -e\rho(\mathbf{R})/|\mathbf{r} - \mathbf{R}|$ and interelectronic repulsion $V_r = \sum_{i<j} e^2/r_{ij}$ operators in the bases of multielectron eigenfunctions constructed for each of the $3d^n$ configurations as linear combinations of Slater determinants projected out as bases for irreducible representations of the C_{3v} group with defined spin. The matrix elements were evaluated in terms of the parameters G_2, G_4, B, C, and the angle β between the outward normal, the metal atom, and the nearest oxygen atom of the silica surface.[22] The G_2 values were assumed to be proportional to G_4 by a factor 2 or 3, and angles β were taken to be those obtained by optimization of the geometry in the DFT calculation, also listed in Table 4.

3.5.2. Density Functional Theory (DFT) Interpretation. In the DFT framework, the interelectronic Coulomb and exchange interactions are explicitly embedded via an external universal functional in the KS equations. The KS orbital energies therefore combine the one-electron picture and a part of multielectron exchange and correlation effects. The total energy is then further evaluated using additional Coulomb and exchange-correlation terms.[13] Thus, in principle, the DFT approach is an accurate, all-electron theory limited only by the choice of basis sets and a universal functional. In contrast, LFT is in essence a perturbative treatment that assumes the periodic trends in the properties of transition metal compounds originate from an interplay between one-electron ligand field energy contributions and exchange correlation in the d-manifold only, all on top of a closed subshell of inner metal and ligand electrons and effective charges. Because of these approximations, the relation between DFT and LFT is far from obvious, but the results presented in Figure 6 show that these two approaches give a satisfactory agreement and an altogether congruent physical picture. The DFT (Figure 6a) and LFT (Figure 6b) energies follow very similar patterns, with some differences particularly in the experimentally "uncharted area" of the adsorbed atomic and bivalent ionic species of vanadium and titanium. Here LFT predicts greater stabilization of V(II) than Ti(II) and DFT yields comparable energies for V(0) and Ti(0). A similar but smaller difference occurs between nickel and cobalt: LFT stabilization of Ni(II) is greater than that of Co(II), and the DFT energies of Ni(0) and Co(0) are comparable with a slight preference for

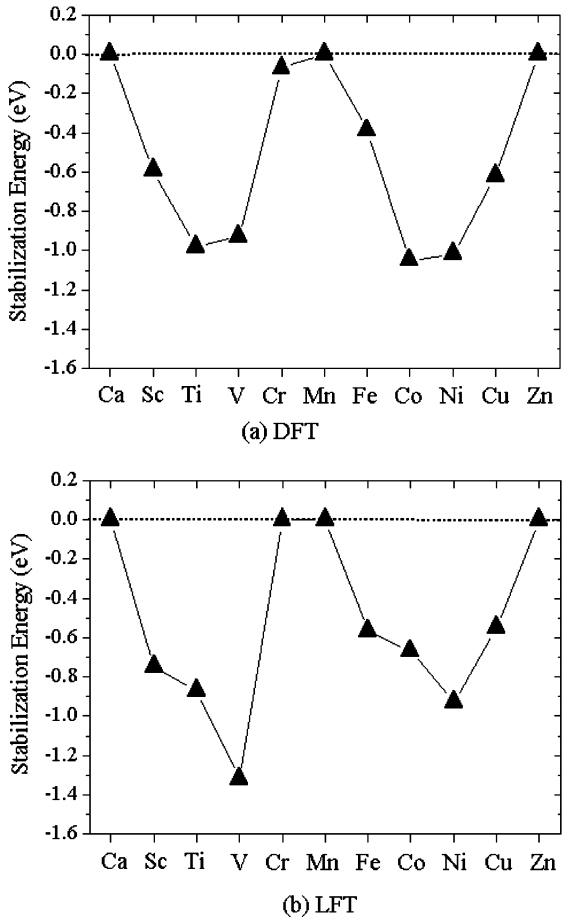

Figure 6. 3d electron contributions to relative stabilization energies: (a) DFT adsorption energies of Me(0) from Figure 5a after subtraction of the smoothly varying background; (b) LFT binding energies of Me-(II) calculated with parameters from Table 4 and $G_2/G_4 = 3$. ($G_2/G_4 = 2$ gives very similar results.)

adsorbed cobalt. This is a consequence of s−d hybridization in zerovalent metals which was discussed in our earlier work.[10]

4. Conclusions

Adsorption energies and interatomic distances of $3d^n4s^{1-2}$ metal atoms on silicon dioxide surface exhibit periodic double-hump patterns determined primarily by the $3d^n$ subshell. In addition, there is an overall trend toward weakening of the metal−oxide bond when passing from early to late transition metals. This trend is due to interaction of progressively contracted 4s electrons of the metal with empty 3s orbitals of silicon and is opposite to that for ions of the same metals. The present all-electron DFT-FPLAPW calculations yield a physical picture that is consistent with semiempirical ligand field theory (LFT) of partially filled d shells when the effects of 4s electrons are taken into account. The pattern includes an important difference between lack of stabilization of Cr(0) atoms due to the promotion of one 4s electron of Cr(0) to make a configuration $3d^54s$ with a half-filled d shell and a large stabilization of Cr(II) ions with partially filled, ligand field stabilized configuration $3d^4$. A reversal of relative stabilization of cobalt and nickel neutral atoms compared to that in bivalent ions has been found to be an effect of d−s hybridization in the adsorbed atoms.

Acknowledgment. This research was carried out under the Grant PIT-189-00 of the Pennsylvania Infrastructure Technology Alliance (PITA) program with financial support from PITA and Air Products and Chemicals, Inc. (APCI). Support of scientists Drs. K. Anselmo, J. Armor, J. Tao, B. K. Heft, and C. Valenzuela and their commitment to computational approaches to practical aspects of material science of catalysis is highly appreciated. A U.S. DOE grant DE-FG26-01NT41276 for theoretical modeling of interfaces is also gratefully acknowledged.

References and Notes

(1) Klier, K. *Langmuir* **1988**, *4*, 13.
(2) Penney, W. G. *Trans. Faraday Soc.* **1940**, *35*, 627.
(3) Hush, N. S.; Pryce, M. H. L. *J. Chem. Phys.* **1958**, *28*, 244.
(4) Siegbahn, P. E. M. *Adv. Chem. Phys.* **1987**, *69*, 447.
(5) Wang, S. G.; Schwarz, W. H. E. *J. Chem. Phys.* **1998**, *109*, 7252.
(6) Bridgeman, A. J.; Rothery, J. *J. Chem. Soc., Dalton Trans.* **1999**, 211.
(7) Klier, K. In *Catalysis by Unique Metal Structures in Solid Matrixes − From Science to Applications*; Bell, A. T., Centi, G., Wichterlova, B., Eds.; NATO Science Series; Kluwer Academic Press: Dordrectht, The Netherlands, 2001; pp 115−133.
(8) Bridgeman, A. J. *J. Chem. Soc., Dalton Trans.* **1996**, 4555.
(9) Bridgeman, A. J.; Bridgeman, C. H. *Chem. Phys. Lett.* **1997**, *272*, 3.
(10) Ma, Q.; Klier, K.; Cheng, H.; Mitchell, J. W.; Hayes, K. S. *J. Phys. Chem. B* **2000**, *104*, 10618.
(11) Ma, Q.; Klier, K.; Cheng, H.; Mitchell, J. W.; Hayes, K. S. *J. Phys. Chem. B* **2001**, *105*, 2212.
(12) Ma, Q.; Klier, K.; Cheng, H.; Mitchell, J. W.; Hayes, K. S. *J. Phys. Chem. B* **2001**, *105*, 9230.
(13) Blaha, P.; Schwarz, K.; Luitz, J. In *WIEN97 User's Guide A Full Potential Linearized Augmented Plane Wave Package for Calculating Crystal Properties*; Karlheinz Schwarz, Ed.; Techn. Universität Wien: Wien, Austria, 1999; ISBM 3−9501031−4.
(14) Hohenberg, P.; Kohn, W. *Phys. Rev. B* **1964**, *136*, 864. Kohn, W.; Sham, L. J. *Phys. Rev. A* **1965**, *140*, 1133.
(15) Perdew, J. P.; Burke, K.; Ernzerhof, M. *Phys. Rev. Lett.* **1996**, *77*, 3865.
(16) Lide, D. R. *Handbook of Chemistry and Physics*, 76th ed.; CRC Press: Boca Raton, FL, 1995.
(17) Ogawa, K.; Nitta, M.; Aomura, K. *Zeolites* **1981**, *1*, 169.
(18) Ogawa, K.; Nitta, M.; Aomura, K. *J. Phys. Chem.* **1978**, *82*, 1655.
(19) Klier, K.; Hutta, P. J.; Kellerman, R. *ACS Symp. Ser.* **1977**, *40*, 108.
(20) Jones, M. M. *Elementary Coordination Chemistry*; Prentice-Hall: Englewood Cliffs, NJ, 1964.
(21) Griffith, J. S. *The Theory of Transition Metal Ions*; Cambridge University Press: New York, 1964.
(22) Hutta, P. J. Ph.D. Thesis, Lehigh University, 1974.